Heterogeneous fatigue damage in a nickel-based single-crystal superalloy unraveled using correlative 3D X-ray technology

Zaifeng Zhou[a], Runguang Li[a], Youkang Wang[b,c], Shilei Li[a], Chao Song[a], Guang Xie[d], Jian Zhang[d], Guofeng Cheng[e], Qiang Feng[a], Jonathan Cormier[f] *, Wenjun Liu[g], Yan-Dong Wang[a,h] *

[a] *Beijing Advanced Innovation Center for Materials Genome Engineering, State Key Laboratory for Advanced Metals and Materials, University of Science and Technology Beijing, Beijing 100083, China*

[b] *Institute of High Energy Physics, Chinese Academy of Sciences (CAS), Beijing 100049, China*

[c] *Spallation Neutron Source Science Center, Dongguan 523803, China*

[d] *Superalloys Division, Institute of Metal Research, Chinese Academy of Sciences, Shenyang, 110016, China*

[e] *Analysis and Testing Center for Inorganic Materials, Shanghai Institute of Ceramics, Chinese Academy of Sciences, Shanghai 200050, China*

[f] *Institut Pprime, UPR CNRS 3346, Physics and Mechanics of Materials Department, ISAE-ENSMA, BP40109, 86961 Futuroscope-Chasseneuil Cedex, France*

[g] *Argonne Photon Source, Argonne National Laboratory, Argonne, IL, 60439, USA*

[h] *Institute for Materials Intelligent Technology, Liaoning Academy of Materials, Shenyang 110004, China*

* *Corresponding authors:*

Yan-Dong Wang (ydwang@ustb.edu.cn)*; Jonathan Cormier* (jonathan.cormier@ensma.fr)

Heterogeneous fatigue damage in a nickel-based single-crystal superalloy unraveled using correlative 3D X-ray technology

Abstract

Nickel-based single-crystal (Ni-SX) superalloys under cyclic stress are susceptible to cracking at stress-concentration sites, eventually leading to low-cycle fatigue (LCF) failure. LCF cracks typically originate from intrinsic defects (e.g., voids and carbides) within solidified dendrites. However, systematic quantitative experimental analyses of defect-mediated local damage remain limited. To thoroughly understand the microscopic origins and evolution of LCF damage, correlated 3D mapping of dendrites across various regions is essential. Here, macroscale micro-computed tomography (μ-CT) was initially used to capture internal interdendritic secondary cracks within bulk DD413 superalloy after LCF testing at 760 °C. Subsequently, a multimodal methodology combining synchrotron 3D microdiffraction (3D-μXRD), high-resolution μ-CT, and electron microscopy was established. This approach allowed precise localization of internal damage zones near interdendritic secondary cracks and detailed mapping of the 3D correlated distributions of dendrites, defects, and residual stress/strain fields within these zones at submicron spatial resolution. Finally, the same approach was applied to specimens subjected to interrupted loading at approximately 40% of the fatigue life to uncover the early damage states of dendrites. The dendrite cores (DCs) and interdendritic regions (IDs) exhibit microscale heterogeneous mechanical responses: nearly defect-free DCs accumulate local irreversible slip along specific slip systems to generate slip bands, while the IDs containing various defects accommodate local microplasticity through the activation of multiple slip systems around these defects. The local tensile stress near defects in the IDs exceeds that in the DC slip band regions by more than threefold, leading to the generation of local damage zones within the IDs. Chain-like defect distributions facilitate the interconnection of these local zones into a continuous damage region, further elevating the overall tensile stress in the IDs. Additionally, geometrically necessary dislocations alone are insufficient as indicators of LCF damage; both the internal stress state and its magnitude must be considered. These experimental results provide critical data and insights for the development of multi-physics fatigue models.

Keywords: Ni-based superalloy; Synchrotron microdiffraction; Low-cycle fatigue; X-ray microscopy; Localized deformation

1. Introduction

Nickel-based single-crystal (Ni-SX) superalloys achieved through directional solidification have been widely used in advanced aerospace engines and industrial gas turbine blades due to their significantly enhanced fatigue resistance, which benefits from the lack of high-temperature slip-prone grain boundaries [1-3]. As demands for higher turbine performance and thermal efficiency increase, the high-temperature endurance of turbine blades faces ever more stringent challenges. The addition of refractory elements such as Mo, W, and Re has been shown to enhance the high-temperature capabilities of superalloys [3-5]. However, due to their low diffusion rates and high atomic mass, these elements intensify the disparity in solidification characteristics between dendrite cores (DCs) and interdendritic regions (IDs) during Bridgman solidification, inevitably leading to microstructural heterogeneity [6, 7]. Solidified DCs generally exhibit a regular γ/γ' microstructure enriched with W, Mo, and Re, while IDs are characterized by a coarser irregular γ/γ' microstructure with segregated elements (primarily Ti, Ta, and Al) as well as most intrinsic defects, such as carbide inclusions, micropores, and residual eutectics [8]. The conventional heat treatments are still insufficient in fully eliminating the dendrite-scale microstructural heterogeneity, and such heterogeneity can greatly complicate the micromechanical response of the alloy under cyclic loading. The accuracy of structural integrity assessments for critical components is thus not guaranteed.

Intermediate-temperature low-cycle fatigue (LCF) failure poses a significant risk to the safe and reliable operation of aerospace engines [9-13]. Studies have demonstrated that intermediate-temperature LCF failure in Ni-SX superalloys is closely linked to intrinsic defects retained in solidified dendrite structures, which act as stress singularities that trigger localized microplasticity and initiate fatigue cracks [9, 10, 14-17]. The complex interactions among multiple defects within IDs complicate local irreversible plastic deformation processes, resulting in considerable variability in LCF life [18-21]. However, conventional macroscopic theories struggle to explain the microscopic heterogeneous LCF deformation phenomena [9, 10, 22], such as defect-mediated stress concentrations, lattice rotations, and dislocation pile-ups, highlighting the need for cross-scale investigations to uncover the underlying micromechanisms. Furthermore, the local three-dimensional (3D) stress/strain distributions and their evolution during LCF loading remain unclear, as conventional characterization approaches cannot non-destructively capture residual strains triggered by heterogeneous deformation. LCF loading induces dislocation self-organization and pile-ups, forming persistent or planar slip bands (PSBs/PLBs) that generate inhomogeneous stress fields and cause lattice rotations [13, 23]. These effects significantly raise the stored energy density in certain slip systems, facilitating damage and crack initiation [24]. To accurately predict and discern microscale fatigue damage, it is crucial to first reveal the stress distributions applied during cyclic loading and the resulting strains. While macroscopic residual strains have been experimentally measured [25], the distribution of local residual strains within DCs and defect-rich IDs during LCF loading remains unknown.

In aviation, frequent inspections and proactive replacements help mitigate the effects of fatigue failure to ensure operation safety. These conservative maintenance routines are however often costly and inefficient. The widely adopted damage tolerance design principles offer a more efficient alternative [26], which integrates non-destructive probes with fatigue fracture theory to ascertain the pre-critical growth rates of embryonic cracks, establishing reliable failure criteria for precise residual strength assessment and inspection intervals [27]. To achieve this, researchers need to thoroughly detect microcracks within in-service components and perform quantitative analyses of the surrounding crystallographic information, typically on a 3D scale. Particular attention is given to gradients in lattice curvature (indicative of the plastic state) and lattice strain (elastic strain along a given crystallographic direction which is reflective of the internal stress state), as these factors can reflect the evolution of local micromechanical fields and serve as critical indicators for predicting microcrack propagation trends [23].

Accurately revealing crystallographic information within specific regions of bulk fatigued Ni-SX superalloys remains challenging with conventional characterization methods. Neutron and standard X-ray diffraction techniques only provide averaged volume information due to their millimeter or submillimeter spatial resolution [28-31]. The latest high-resolution electron backscatter diffraction (HR-EBSD) provides the high angular and spatial resolution necessary for surface strain analysis but typically relies on focused ion beam (FIB) serial sectioning for 3D-scale analysis, a process that unavoidably induces stress relaxation [32, 33]. More critically, the absence of a 3D perspective introduces considerable uncertainty when studying microcrack propagation in relation to structural features. Achieving a high spatial and angular resolution to non-destructively uncover crystallographic details within targeted regions of bulk fatigued Ni-SX superalloys is also a challenge for the present study.

In recent years, various 3D X-ray techniques have become increasingly integral to materials research, enabling non-destructive, spatially resolved analysis of microstructures within materials for a deeper understanding of their structure and properties. Notable examples include X-ray computed tomography (X-CT) [34], 3D X-ray microdiffraction (3D-μXRD) [35], diffraction contrast tomography (DCT) [36], and dark-field X-ray microscopy (DFXM) [37]. Among these, synchrotron-based 3D-μXRD offers both high spatial (< 500 nm) and angular (< 0.01°) resolution, making it ideal for capturing ultra-low-strain deformation and stress localization within bulk metals [38]. Nevertheless, the structural heterogeneity, complex internal stress states, and localized fatigue damage in Ni-SX superalloys complicate diffraction signal analysis in 3D-μXRD, potentially reducing result reliability and risking the omission of critical features. X-CT with micro- or sub-micron resolution (μ-CT) offers high efficiency and broader coverage and has been proven effective for detecting intrinsic defects and microcracks in bulk metals [38, 39]. As such, μ-CT can guide 3D-μXRD measurements to ensure critical features are captured and assist in distinguishing and analyzing internal diffraction signals. The combined use of the two 3D X-ray techniques enables precise localization of fatigue-sensitive zones and provides reliable insights into microscopic deformation mechanisms.

In this study, we present the submicron-scale 3D correlative distributions of residual stress/strain fields, dendritic microstructures, defects, and dislocation configurations in Ni-SX superalloys subjected to intermediate-temperature LCF loading. This work aims to elucidate the heterogeneous fatigue damage mechanisms within monocrystalline dendritic structures, providing a detailed description of defect-mediated incompatible deformation and quantitatively confirming the mechanical heterogeneity between DCs and IDs. A novel multimodal analytical framework that integrates synchrotron 3D-μXRD and μ-CT techniques with submicron spatial resolution has been strategically established. This correlative approach enables precise acquisition, subdivision, and integration of crystallographic orientations and elastic strains within target regions of bulk Ni-SX superalloys, facilitating accurate localization and quantification of internal damage in cast alloys with solidification dendritic structures. This study significantly deepens our understanding of the microscopic origins and progression of embryonic crack nucleation and subcritical growth driven by stress/strain localization around defects under intermediate-temperature LCF loading, underscoring its fundamental scientific and practical importance.

2. Experiment

2.1. Material description and fatigue test

The nominal composition of the DD413 alloy is listed in Table 1. DD413 rods with a diameter of 16 mm were directionally solidified along the [001] orientation using the spiral grain selection method in a vacuum directional solidification furnace (Bridgeman process). A two-stage solution heat treatment was applied (1230 °C for 2 hours followed by 1250 °C for 4 hours), followed by a precipitation hardening treatment at 1080 °C for 4 hours. The primary misorientations of the single-crystal rod axes relative to the [001] orientation were determined via EBSD, and rods with deviations within 5° were selected for further fatigue testing. The cylindrical dog-bone shape specimens machined from the heat-treated rods were prepared with a gauge length of 14 mm and a diameter of 6 mm. Before testing, mechanical and electrochemical polishing were conducted to eliminate surface-machined scratches and work hardening inherited from the machining process to avoid any possible recrystallization during fatigue straining. Fatigue tests were conducted at 760 °C under total strain control of $\Delta\varepsilon_t/2 = 1.1\%$ along the [001] orientation using a servo-hydraulic testing machine (MTS Series 809 A/T). A triangular waveform at a constant strain rate of 5×10^{-3} s^{-1} and a strain ratio of $R = -1$ was utilized, with total strain monitored by an extensometer on the specimen ledges. Temperature fluctuations across the gauge length were maintained within ±3 °C. Tests were performed to failure, with additional interruptions at approximately 40% of the expected lifespan. Completed samples were air-cooled to room temperature under a constant 10 MPa load. Four specimens were tested on the same machine to ensure data stability and minimize equipment-induced variance. Further details on the alloy microstructure and LCF damage at different strain amplitudes are available in Ref. [8].

2.2. Micro-computed tomography

μ-CT scans were acquired using an X-ray microscope (XRM, YXLON FF35CT) operating at 180 kV, achieving a voxel resolution of $3.86 \times 3.86 \times 3.86$ μm^3. A rod sample with a 3 mm diameter was extracted from the middle of the gauge section of the failed specimen. X-ray projection images were recorded with an exposure time of 1.2 seconds per image, typically capturing 1801 images during a stepwise specimen rotation. The acquired data were reconstructed using VG Studio Max to reduce noise and enable 3D visualization, while Avizo software was used to segment microcracks and intrinsic defects via grayscale thresholding for further analysis. Longitudinal projection images parallel to the loading direction were generated from the reconstructed dataset to highlight key fatigue cracking features. The selected cross-section was meticulously positioned and manually ground to expose it for subsequent inspections. Vickers indentations (~15 μm) were used to mark the start and endpoints of a transverse synchrotron scan and indicated the X-ray penetration direction. The marked region was subsequently identified using a field emission gun scanning electron microscope (FEG-SEM, Zeiss Gemini 450) at 20 kV, with a 20-minute surface irradiation that caused minimal damage (a few nanometers) to create visible markers. A thin slice sample ($1 \times 1 \times 0.5$ mm^3) was then extracted using electric discharge machining, positioning the burned area near the sample center. High-resolution μ-CT scans of the extracted slice were conducted with an XRM (Zeiss Xradia 620 Versa) at 140 kV, achieving a voxel resolution of $1.18 \times 1.18 \times 1.18$ μm^3. The sample was mounted using an aluminum tube adapter and rotated 360° with discrete angle pauses for 2D projection imaging, capturing 991 exposures at 1 second each. Data were reconstructed using ORS Dragonfly software, and Avizo was utilized for visualization and data registration. Noise reduction was accomplished using median filtering [40], with data points smaller than two voxels excluded during threshold segmentation to enhance clarity and accuracy.

2.3. Electron microscopy

EBSD scans were conducted using an FEG-SEM (Zeiss Gemini 450) equipped with a CMOS symmetry EBSD detector, operating at 20 kV with step sizes of 0.2 to 1.0 μm. Analyses of orientations, slip traces, and geometrically necessary dislocations (GNDs) were performed using AZtecCrystal software and custom MATLAB code based on the MTEX toolbox [41]. Specimen preparation involved meticulous mechanical grinding followed by vibration polishing. For a detailed examination of the microstructure and dislocation configurations, imaging was performed using a bright-field (BF) detector (scattering angle: 9 mrad) and a low-angle annular dark-field (LAADF) detector (DF2, scattering angle: 12~19 mrad) on a 200 kV scanning transmission electron microscope (STEM, FEI Talos F200X). Thin foils near the crack tip were prepared using a dual-beam FIB instrument (FEI Helios Nano Lab 600i). A 1.0 μm platinum protective layer was deposited with a 12 kV ion beam to safeguard the cross-sectional surface. The thinning process was optimized by first using a high-energy ion beam (30 kV), followed by a low-energy ion beam (2 kV) to remove any amorphous regions, yielding final lamellae approximately 80 nm thick. Additional electro-polishing was carried out using a twin-jet polisher with a solution of 10% perchloric acid and 90% ethanol at -30 °C and 30 V.

2.4. Three-dimensional X-ray microdiffraction

The 3D-μXRD measurements were performed at beamline 34-ID-E of the Advanced Photon Source, Argonne National Laboratory (APS, ANL), US. A polychromatic X-ray beam with energies ranging from

7 to 30 keV was focused into a 0.3 μm × 0.3 μm spot using a Kirkpatrick-Baez mirror pair. Overlapping Laue diffraction patterns, generated by the penetration of the X-ray beam through the specimen, were recorded on a 2048 × 2048 pixel Perkin-Elmer area detector (pixel size: 200 μm × 200 μm) positioned 0.5 m above the sample in a 90° reflection geometry. Depth resolution was achieved by scanning a 100-μm-diameter platinum wire across the sample surface, serving as a differential aperture. Triangulation enabled the identification of diffracted rays, providing a depth resolution of 0.5 μm. A horizontal X-ray line scan was performed approximately 4 mm from the fatigue crack region and perpendicular to the loading direction, covering a scanning length of 400 μm with a step size of 1.0 μm, reaching a penetration depth of about 100 μm. Slices inclined at a 45° angle to the specimen surface were measured via depth-resolved line scanning. An additional horizontal scan was conducted near the gauge section midpoint of a specimen at ~40% of its fatigue life, covering 250 μm with 1 μm steps. Depth reconstruction and indexing of Laue patterns were completed at APS using the LaueGo software. Post-processed crystallographic data, including crystallographic orientations, grain boundaries, GND densities, slip traces, and elastic strain components [42], were analyzed using in-house MATLAB code. High-angle grain boundaries (HAGBs) were defined with a misorientation threshold of 10°, and kernel average misorientation (KAM) was evaluated using a 3 × 3 kernel size with a 2° cut-off angle. The minimum total GND densities were calculated following methodologies proposed by Pantleon [43] and Muránsky [44]. Potential variations in lattice rotation gradients perpendicular to the scan surface were disregarded, and the calculation relied on the minimum line energy criterion. Despite the influence of elastic strain gradients on Nye's dislocation tensor [45], the magnitude of the lattice curvature change induced by it is considerably lower than that resulting from the measured rotation gradients. Thus, GND densities were derived from the six available rotation gradients [46]. Denoising of crystal orientation maps was performed using variational methods [47]. The elastic strain gradients, calculated similarly to KAM, were assigned to the central pixel based on the average differences among neighboring pixels within a 3 × 3 kernel. The mean reference orientation deviation angle (MROD-ω) was calculated as the misorientation between each pixel's orientation and the average orientation of all pixels. Lattice rotation axes for MROD-ω were visualized on a color-mapped sphere representing the specimen frame, with separate color keys for the upper and lower hemispheres.

3. Results

3.1. Fatigue microcracking

Supplementary Fig. S1 presents the tension-compression LCF curve of the DD413 alloy at 760 °C under ±1.1% strain control with the loading direction along the [001] crystallographic axis. The specimen initially exhibited strain hardening for the starting 10 cycles, followed by cyclic softening until failure after 268 cycles. Additional tests were interrupted at 98 cycles (corresponding to 40% fatigue lifetime) to investigate early-stage fatigue damage. As shown in Fig. 1, a miniature sample was extracted from the gauge section (starting at the fracture surface) of a post-mortem dog-bone-shaped specimen subjected to 268 cycles to enhance spatial resolution during μ-CT imaging. Carbide inclusions in the extracted specimen display a regular chain-like distribution at specific intervals, primarily situated in IDs. Two zig-zag secondary cracks extending from the fracture surface into the interior were also captured (Fig. 1). A detailed comparison between the magnified crack path and the distribution trajectory of chain-like intrinsic defects reveals that the crack initially propagated along the right-side ID before deflecting toward the left ID, as indicated by orange dashed lines in Fig. 1. These 3D observations offer a more reliable identification of microstructural components or regions in DD413 alloys prone to damage accumulation and cracking under LCF loading.

The reconstructed miniature specimen was sectioned at 4 μm intervals along the X-Y plane to show the secondary cracks and microstructural features, as displayed in Fig. 2. A selected tomography slice reveals crack growth characteristics along chain-like intrinsic defects, where white particles represent carbide inclusions and black microregions correspond to micropores (Fig. 2). This slice was located and carefully polished for EBSD characterization, with the inverse pole figure (IPF), MROD-ω, and GND density maps presented in Fig. 3a-e. Low-angle grain boundaries (LAGBs) are evident in the IDs where the two cracks are situated (Fig. 3a), alongside a notable increase in MROD-ω (Fig. 3b). The microcrack growth path follows the trace of an FCC {111} crystallographic plane, marked by the black dashed line in Fig. 3c. Randomly oriented carbide inclusions are observed to the right of the crack path.

Near the microcrack, LAGBs and high-density GNDs extend alongside the crack path to its tip before deflecting toward two carbides approximately 30 μm apart, suggesting a potential trend for further microcrack propagation (Fig. 3d and e). Supplementary Fig. S2 provides additional details of the fatigue crack regions, highlighting two critical features: (i) the presence of carbides at the crack path deflection sites and (ii) an MROD-ω increase of over 2° near these carbides, underscoring their significant role in microcrack initiation and propagation under LCF. Contrasting to the ID where the fatigue crack originates, the neighboring defect-free DC exhibits minimal microplasticity (Fig. 3e). It is necessary to note that EBSD provides only a conservative estimate of dislocation density [43, 44], as it cannot measure statistically stored dislocations (SSDs) that contribute to strain hardening, nor can it visualize dislocation configurations. TEM foils were further prepared from specific sites of the DC and ID, as displayed in Fig. 3d. Location A in the DC reveals a lower dislocation density, consistent with EBSD results, with most dislocations confined to the softer γ channels instead of shearing the γ' phase (Fig. 3f and g). In contrast, location B within the ID shows a higher dislocation density near the carbide, where dislocation entanglements in the γ channels begin to shear the γ' phase, as displayed in Fig. 3h and i. These findings highlight the local stress variations due to inconsistent micromechanical responses of DCs and IDs under LCF loading, manifesting as dislocation entanglements in the γ channels and slip activity within the γ' ordered phases [48].

3.2. Lattice orientation field in fatigued microstructures

The correlative 3D X-ray microscopy integrating 3D-μXRD and μ-CT was employed to analyze lattice rotation and elastic strain in fatigued microstructures within a 1.5 mm thickness specimen containing the selected slice (Fig. 3a), positioned approximately 4 mm from the fatigue crack region (Fig. 4a). A transverse 3D-μXRD scan was conducted at a 45° angle to the specimen surface, spanning ~400 μm along the X direction (penetrating ~100 μm) and oriented perpendicular to the loading axis (Fig. 4a). Post-processing of Laue patterns at different depths revealed three void regions without diffraction signals, identified as micropores (Supplementary Fig. S3c), with one representative Laue pattern shown at point 2 in Supplementary Fig. S4. A high-resolution μ-CT scan of a $1 \times 1 \times 0.5$ mm^3 region surrounding the synchrotron scan trace aided in analyzing diffraction signals. The identification, labeling, and extraction of this trace for high-resolution μ-CT imaging are detailed in Supplementary Fig. S3a and b. Two-dimensional (2D) slices from the reconstructed high-resolution μ-CT dataset aligned with the penetration direction and depth of the 3D-μXRD scan were generated for data registration, identifying the 3D-μXRD scanning range within the bulk interior based on spatial distances among the three voids, as displayed in Supplementary Fig. S3c. The range spanned three IDs and two DCs from left to right (outlined by black dashed lines on the transparent cross-section in Fig. 4b), with voids 1, 2, and 3 located within the IDs. The 3D morphology of the three microvoids shows considerable size variation (Fig. 4c), and minor deviations in slicing angle may cause discrepancies in void morphology on the 2D slices, as illustrated in Supplementary Fig. S3c.

Fig. 5a-e presents a series of maps depicting lattice orientation derived from Laue patterns after depth reconstruction. By estimating the proportions of DCs and IDs in the μ-CT slices shown in Fig. 4b, the IPF-Y map within a ~1° range (Sharp-IPF-Y) was subdivided along black dashed lines, unveiling notable lattice orientation fluctuations within the three IDs (ID1, ID2, and ID3), whereas the two DCs (DC1 and DC2) displayed homogeneous lattice orientations (Fig. 5a). In the IDs, localized zones exhibit misorientations exceeding 10° (indicated by gray HAGBs), possibly associated with MC-type carbide inclusions (Fig. 5a). TEM analysis confirmed that most carbide inclusions in this alloy share the Fm-3m space group with the Ni phase (Supplementary Fig. S5), allowing them to be indexed, but their Laue patterns are markedly distinct from those of the matrix (Supplementary Fig. S4). Detailed crystallographic parameters for both the carbides and the matrix are summarized in Table 2. The GND density in ID1 through ID3 is notably elevated due to carbide inclusions, reaching values up to 1.1×10^{14} m^{-2} between two carbides in ID1, suggesting the role of carbide clusters in accommodating plastic deformation within the surrounding matrix (Fig. 5b). In contrast, DC1 and DC2 display low and uniform GND density values, with DC1 recording a lowest value of only 1.7×10^{12} m^{-2}, indicating homogeneous deformation in these regions (Fig. 5b).

Fig. 5c and e depict the MROD-ω map and rotation axis map generated with high angular resolution via 3D-μXRD technology, indicating the lattice rotation distinctions between the DCs and IDs. MROD-ω values are consistently low and uniform in DCs, ranging from 0.16° to 0.22° (Fig. 5c). In contrast, IDs show notable fluctuations with high (exceeding 1°) and low (below 0.1°) rotation angles concentrating and departing from intrinsic defects (Fig. 5c). The derivative of MROD-ω along the X-direction (Fig. 5d) further provides a quantitative assessment of the plastic deformation gradient within the analyzed region (highlighted by the transparent white area in Fig. 5c), revealing that ID2 and ID1 which are closest and furthest to intrinsic defects displays the sharpest and moderate plastic deformation gradients, and ID3 falls in between (Fig. 5c and d). Both defect-free DCs show only minor gradients, indicating that regions closer to intrinsic defects undergo more heterogeneous deformation for local mechanical accommodation (Fig. 5c and d).

Fig. 5e presents a rotation axis map where each spot signifies a specific axis on a colored sphere corresponding to MROD-ω in the specimen frame. Consistent coloring in DC1 and DC2 indicates shared rotation axes for MROD-ω within these subdivided zones, implying minimal local lattice rotations and limited heterogeneous deformation in the DCs during LCF loading. In contrast, the three IDs exhibit clear coloring subdivisions, especially around intrinsic defects, with a noticeable divergence in axis projection distributions. Simultaneously, the alignment of interfacial boundaries among multiple color blocks with the superimposed {111} traces (red lines marking the alignment plane traces) implies the activation of multiple slip systems within the IDs [49] (Fig. 5e).

3.3. Dislocation configurations in fatigued microstructures

TEM was used to analyze the dislocation configurations of DCs and IDs with the results presented in Fig. 6. The TEM-imaged electron beam-transparent region was located near the lower side of the 3D-μXRD cross-section. In the DCs, dislocations having a Burgers vector of $a/2[0\bar{1}1]$ (through dual-beam visibility analysis [48] as indicated by the white arrow in Fig. 6b) were observed to align unidirectionally at regular intervals along the $(\bar{1}11)$ plane under the [110] crystallographic zone axis (Fig. 6a), which arises from local irreversible $(\bar{1}11)[0\bar{1}1]$ slip upon LCF loading. This process begins with the random capture and storage of dislocations in the low-strength γ phases [50], followed by a rising dislocation density as plastic strain accumulates, leading to dislocation entanglement (Fig. 6c) and eventually initiating γ' phase shearing [48]. Despite these activities, the overall dislocation density in the DCs remains relatively low, with dislocations primarily concentrated near the slip bands, which decrease as the distancing from the slip bands increases.

The γ' particles in the IDs display coarsening and irregular morphologies and are accompanied by numerous carbide inclusions (Fig. 6d). Unlike in the DCs, where slip bands are well-defined, the IDs feature entangled dislocations within the γ channels and bidirectional arrangements of super-dislocation pairs along the $(1\bar{1}1)$ and $(\bar{1}11)$ planes within the γ' phase. The $a/2[0\bar{1}1]$ and $a/2[\bar{1}01]$ dislocations, as marked by white arrows in Fig. 6d and e, were identified. Additionally, one dislocation with a Burgers vector different from the above was also identified near a carbide inclusion in the γ' phase (indicated by a white triangle), suggesting the activation of other assisting slip systems beyond $(1\bar{1}1)[\bar{1}01]$ and $(\bar{1}11)[0\bar{1}1]$, as illustrated in Fig. 6e. An interfacial dislocation array between the carbide and the matrix reflects how the matrix accommodates deformation around the plastically rigid inclusions (Fig. 6f). This dislocation configuration in the IDs arises from the physical and mechanical property disparities between the matrix and intrinsic defects, necessitating the activation of additional slip systems to reconcile incompatible deformations under cyclic loading. Dislocations from multiple slip systems are further activated as deformation progresses, leading to stronger interactions, shorter slip distances, more dislocation pile-ups [48, 49], and severe stress localization. These findings were reproducible across electron beam-transparent areas encompassing several DCs and IDs. Although not all regions were fully analyzed, evidence indicates that at least two identical slip systems were active within the IDs, as inferred from dislocations aligned in the same directions and becoming invisible under identical reflections.

3.4. Elastic strain field in fatigued microstructures

Fig. 7a-d displays maps related to elastic strain tensors to unveil the local stress states in fatigued microstructures. One representative normal elastic strain component (ε_{yy}) and one shear elastic strain component (ε_{zy}) are selected for detailed analysis (the remaining four components ε_{xx}, ε_{zz}, ε_{xy}, ε_{zx} are available in Supplementary Fig. S6). Note that to illustrate the relationship between stress states and crack paths intuitively, the directions of these strain components are shown in the sample frame in Fig. 7a. In regions DC1 and DC2, ε_{yy} and ε_{zy} exhibit relatively low strain levels, with localized zones showing elevated tensile or compressive strain values in a subtle banded distribution (Fig. 7b and c), which align with the red {111} traces (Fig. 5e). In contrast, strain levels of both ε_{yy} and ε_{zy} are significantly higher in the three IDs, with localized strain enhancements particularly pronounced near intrinsic defects (Fig. 7b and c). Additionally, the maximum tensile elastic strain of 9.6×10^{-3} observed between two carbides in ID1 exceeds the 7.1×10^{-3} tensile strain between the void at the top and the adjacent carbide, which is due to the more inhomogeneous deformation in the matrix surrounding carbide clusters than regions near voids (Fig. 5b and 7b). The role of these intrinsic defects in LCF damage accumulation will be further explored in Section 4.1.

The change of micromechanical fields is often linked to the generation of specific dislocation configurations in localized zones, such as strain gradients from incidental dislocation boundaries (IDBs) and orientation gradients from geometrically necessary boundaries (GNBs) [44]. In the ID2 region, a subdivided yet interconnected zone of elevated tensile and compressive elastic strains is observed between two carbides approximately 50 μm apart, arising from dislocation pile-ups at the mesoscopic scale, as illustrated in Fig. 7b and further highlighted by the magnified view within the black dashed box in Fig. 7c. The compressive strain zone corresponds to one side with an extra half atomic plane, while the tensile strain zone forms on the opposite side [23, 51], as illustrated in Fig. 7d. This dislocation configuration gives rise to a localized damage zone, where the tensile strain region reflects a long-range tensile stress state that facilitates damage under external loading, accompanied by a substantial elastic strain gradient (ε_{zy} Grad) extending 5~8 μm along the depth direction. Meanwhile, quantitative analysis of this zone (marked by rectangles and arrows in Fig. 7d$_2$ and d$_3$) indicates a maximum KAM variation of only 0.07°, compared to a ε_{zy} Grad variation exceeding 6×10^{-3}, designating it as a potential site for fatigue crack initiation and propagation, as illustrated in Fig. 7e. It is worth mentioning that such analysis is made possible by the high angular resolution of 3D-μXRD technology, which is beyond the reach of conventional EBSD techniques. Moreover, the elastic strain distribution in the DCs and IDs after intermediate-temperature LCF loading was statistically analyzed, revealing that intrinsic defects in the IDs (ID1~ID3) induce a higher proportion of regions with elevated tensile elastic strain values (ε_{yy} ranging from 4×10^{-3} to 8×10^{-3} and ε_{zy} from 5×10^{-3} to 9×10^{-3}) compared to the DCs (D1 and D2). The increased localized tensile elastic strain accounts for the higher frequency of fatigue cracks observed in the IDs, as displayed in Fig. 8a and b.

3.5. Early fatigue damage of microstructures

The lattice orientation field within the ~40%-fatigue-interrupted sample (at the early fatigue stage) is shown in Fig. 9a-d. The multimodal analysis segmented the Sharp-IPF-Y map (within ~1°) into two regions: a nearly defect-free DC on the left and an ID on the right containing carbide inclusions and micropores (Fig. 9a). At the early fatigue stage, the DC region is characterized by parallel bands approximately 7 μm wide with highly close lattice orientations, indicative of localized irreversible slip along a specific slip system. The MROD-ω values between these bands remain below 0.2°, signifying minimal orientation gradients within the DC (Fig. 9c). In contrast, the ID exhibits substantial orientation variation, particularly near intrinsic defects (Fig. 9a). Local lattice rotations in these regions exceed 0.5° with varying rotation axes (Fig. 9c and d), indicating the early onset of marked heterogeneous deformation within the ID.

Fig. 10a-f depicts maps of six elastic strain components of the microstructure during the early stages of LCF loading. In the DC, banded zones with elevated local elastic strain are clearly visible (Fig. 10a-c). Conversely, high strain values are primarily localized around intrinsic defects in the ID, while regions farther from these defects exhibit significantly lower strain levels, with slip band features nearly absent (Fig. 10a-c). The DC primarily accumulates local irreversible slip along specific slip systems, whereas the ID undergoes incompatible deformation (Fig. 9b). Both the elastic strain levels and the proportion of high-elastic-strain regions in the ID are relatively lower than the post-mortem specimen (Fig. 7b and 10b). Additionally, regions of elevated tensile elastic strain near carbide clusters in the ID are nearly interconnected with adjacent DC slip bands (Fig. 10b). This connectivity likely explains the tendency for interdendritic cracks to deflect into the DCs, enabling alternating propagation between neighboring IDs (Fig. 1).

4. Discussion

In this study, we established a multimodal analytical framework that integrates synchrotron 3D-μXRD, μ-CT, and advanced electron microscopy to map the submicron-scale spatial correlations among 3D residual stress/strain fields, dendritic structures, defects, and dislocation configurations within bulk Ni-SX superalloys during the early stages of fatigue and post-failure. This approach quantitatively and statistically reveals the mechanical heterogeneity in fatigue damage between DCs and IDs. This section first discusses the LCF damage behavior of Ni-SX superalloys at intermediate temperatures, with a focus on carbide effects, then compares damage levels between DCs and IDs to clarify the microscopic origins and evolution of heterogeneous fatigue damage. Finally, the broader applicability of this multimodal analytical approach to other cast alloys with dendritic structures is discussed.

4.1. The impact of intrinsic defects on LCF damage

The present research highlights the significant role of carbide morphology in LCF damage accumulation, particularly when the orientation of carbide tips or sharp edges (those most likely to induce localized plastic deformation) aligns with the external loading axis, thereby increasing the likelihood of fatigue crack initiation [9, 46]. This effect is corroborated by the locally elevated GND density and tensile elastic strain observed at sharper carbide corners compared to more rounded ones, as indicated by white arrows in ID1 of Fig. 5b and 7b. Moreover, the GND density and tensile elastic strain are notably higher around carbide clusters than around isolated carbides (as shown in ID2 of Fig. 5b and 7b and the ID regions of Fig. 9b and 10b), which could explain the frequent occurrence of LCF cracks in regions with mesh-like or chain-like carbide distributions reported in previous studies [10, 16, 52, 53]. Attempts to correlate carbide morphology with local effective strain and GND distribution through finite element analysis have been made [46]. These proposed models however often rely on data from random 2D plane examinations, which may introduce incalculable uncertainty in their predictions due to the lack of robust experimental validation. Given the complex 3D morphology of carbides (Fig. 4b and c), such 2D constraints fail to capture critical details, further compromising modeling accuracy. Future studies should focus on incorporating more comprehensive 3D analyses to improve the reliability of fatigue life prediction models.

Previous work has indicated that carbides can activate multiple slip systems in the surrounding matrix, resulting in pronounced heterogeneous deformation [46]. Similarly and more deeply, our work reveals that local lattice rotations near carbides along different crystallographic axes (Fig. 5c and e) arise from the activation of multiple slip systems in the matrix to accommodate local microplasticity around these rigid carbides as directly evidenced by the dislocation configurations (Fig. 6d-e). While carbides generally enhance fatigue resistance in superalloys by hindering dislocation motion (both SSDs and GNDs) [9], our observations show that when carbides obstruct local irreversible slip along specific slip systems, dislocation pile-ups can form, leading to an elevation in local tensile strain/stress levels that substantially increase fatigue cracking risk. Consequently, optimizing alloy composition and refining the casting process to control carbide morphology and distribution - avoiding network or chain-like arrangements - could reduce stress concentrations and postpone damage accumulation under intermediate-temperature LCF conditions.

4.2. Quantitative comparison of fatigue damage between DCs and IDs

Fig. 11 quantitatively compares the fatigue damage modes between DCs and IDs during the early stages of LCF loading. Fig. 11a shows the crystallographic orientation at Point A from Fig. 9a (expressed as Euler angles) alongside the calculated {111} slip traces. Fig. 11b presents the Schmid factors for all twelve slip systems, with the slip system having the highest Schmid factor highlighted. In the DCs, the overall tensile components of ε_{yy} remain relatively low, typically below 1500 με (Fig. 11c). Notably, the largest local strain peaks coincide with the red slip traces, indicating activation of the $(111)[1\bar{1}0]$ slip system with the highest Schmid factor, while smaller peaks correspond to the blue slip traces (Fig. 11c). In contrast, the tensile components of ε_{yy} in the IDs are higher, with prominent regions exceeding 3000 με and showing random orientations. Statistical analysis of ε_{yy} along Paths B and C in Fig. 10b confirms that local stress concentrations arising from intrinsic defects in the IDs are more pronounced than the slip band formation within the DCs under LCF (Fig. 11c). Using the approach outlined in Ref. [54], which assumes that the three principal stress directions align with the sample's coordinate axes (X, Y, and Z), the relative residual stress values parallel to the loading direction at the positions marked by the black arrows in Fig. 11c were quantitatively compared. The Poisson's ratio and elastic modulus were taken from Ref. [55]. The results show that the residual stress in the DCs is 139 MPa, whereas in the IDs it reaches 458 MPa, indicating that the local damage level in the IDs is over three times higher than that in the DCs. These high-tensile stress zones in the IDs when superimposed with the externally applied tensile load serve as potential sites for crack nucleation.

Recently, the concept of GNDs has been more frequently used to explain the LCF crack initiation and propagation mechanisms of superalloys containing inclusions [9, 10, 18, 56]. Regarding crack initiation, some studies suggested that GND accumulation contributes to strain hardening and increases local shear stress, potentially promoting crack initiation through energy storage and dissipation [57, 58]. However, others argued that GND density alone is insufficient to predict crack initiation sites reliably, as elevated GND density levels are not exclusive to these regions [56]. We believe that incorporating the analysis of internal stress states in the corresponding regions can strengthen the robustness of LCF damage indicators. Along Path A (highlighted by dashed lines in Figs. 9b and 10b), a quantitative correlation between the distributions of ε_{yy} and GND density was established (Fig. 12). Within the DCs, three tensile strain peaks were identified at approximately 11 μm intervals, corresponding to slip band regions (regions 1, 2 and 3 marked in light yellow). This spacing closely matches the shear band spacing (9~12 μm) measured by high-resolution digital image correlation (DIC) in Ref. [59], although the measured strain values are lower than those reported in the literature. This discrepancy likely reflects both the early stage of deformation and differences in measurement tools, as displayed in Fig. 12. In the slip band regions, GND density peaks exhibit elevated values at the edges and a dip at the center, indicating a pronounced orientation gradient at the slip band edges and a smaller gradient within the band interior (Fig. 12). This observation is consistent with the DIC and crystal plasticity finite element simulation results reported in Ref. [24]. Notably, the highest tensile elastic strain occurs at the GND density trough (i.e., within the slip band itself), revealing a micron-scale offset between the regions of maximum tensile strain and those with the largest orientation gradients. Within the IDs, both the ε_{yy} and GND density distributions exhibit significant fluctuations and elevated values (Fig. 12). In some areas (e.g., regions 4, 6, and 7), the peaks of GND density and ε_{yy} nearly coincide. However, the highest ε_{yy} peak in region 6 (exceeding 5000 με) signals a high crack nucleation risk. Conversely, the highest GND peak appears in region 5, where compressive strain partially counteracts the externally applied tensile load, reducing crack initiation risk. Overall, incorporating the local stress state enhances the accuracy of LCF damage prediction and identification.

Additionally, Guo et al. [24] employed stored energy density resolved on individual slip systems to predict crack nucleation sites, demonstrating a robust and generalizable damage indicator. In our study, we found that in the DCs, once the critical resolved shear stress of a favorable slip system is reached, local irreversible slip accumulates and forms slip bands. This finding is consistent with Ref. [24], where multiple favorable slip systems activate near a notch, leading to the emergence of localized deformation bands and eventual crack initiation. Hence, the stored energy density approach shows promise in predicting cracking in DCs. However, in the IDs, heterogeneous deformation dominates due to the presence of defects with varying types, sizes, and morphologies. The local microplastic behavior varies around these defects, emphasizing the need for further microscale validation to determine whether slip-system-resolved stored energy density can reliably predict crack initiation in IDs. To some extent, elastic strain reflects the magnitude of stored strain energy, capturing the potential energy accumulated after heterogeneous deformation. Thus, it can serve as a valuable indicator for damage prediction in IDs.

4.3. Mechanisms of mechanical heterogeneous fatigue damage in dendritic structures

Based on the quantitative results and microstructural observations presented earlier, we now detail the microscopic origins and evolution of mechanical heterogeneity of fatigue damage within the DCs and IDs of Ni-SX superalloys under intermediate-temperature LCF conditions (Fig. 13a). In the DCs, the relatively homogeneous microstructure and the absence of significant stress singularities enable local irreversible slip accumulation along specific $\{111\}\langle 110\rangle$ slip systems, resulting in the generation of slip bands without triggering local lattice rotations, as evidenced by the consistent orientation observed within DCs (Fig. 5a and 9a). Conversely, IDs experience varying degrees and directions of matrix rotation near intrinsic defects to accommodate lattice curvatures caused by incompatible deformations. This results in variational lattice orientations in these regions (Fig. 5a and 9a), accompanied by dislocation pile-ups (Fig. 7d) and overall elevated tensile elastic strain levels (Fig. 8a and b). This heterogeneity in fatigue damage facilitates the extensive propagation of fatigue cracks initiated in the IDs, as illustrated in Fig. 13b. Intrinsic defects lower the local stress intensity threshold of the surrounding matrix [60], triggering strain localization and forming fatigue damage zones. Additionally, the chain-like distribution of intrinsic defects fosters the interlinkage of these localized damage zones, ultimately driving continuous fatigue cracking. This finding provides foundational insights and experimental evidence to guide further modeling efforts and enhance the understanding of LCF damage behavior in single-crystal superalloys.

This heterogeneous LCF damage micromechanism primarily applies to cast Ni-based superalloys with solidification monocrystalline dendritic structures, where the IDs are rich in defects and the DCs are nearly defect-free. In other cast monocrystalline Ni-based superalloys with different crystallographic orientations, local variations in critical resolved shear stress may cause irreversible slip to accumulate along different, more favorably oriented slip systems within the DCs. When dislocation climb is absent, the microscopic mechanical response in the DCs remains largely unchanged, while in the IDs, irreversible slip is still hindered by defects, leading to heterogeneous deformation.

However, the applicability of this heterogeneous LCF damage micromechanism to cast polycrystalline Ni-based superalloys may be limited. Studies have shown that dendritic structures exhibit distinct microscopic mechanical responses depending on grain size and crystallographic orientation. For instance, local lattice rotations tend to occur in the IDs of large grains with Brass-type orientations and low Schmid factors, whereas small grains with high Schmid factors display markedly different microscopic deformation behaviors [9]. Additionally, grain boundaries can hinder the accumulation of local irreversible slip on specific slip systems, further complicating the microscale deformation behavior of dendritic structures. Consequently, comprehensive investigations focusing on grain size, crystallographic orientation, and grain boundaries are needed to broaden the applicability of this micromechanism. Based on the findings of this study, the average tensile elastic strain ε_{yy} in the IDs could serve as a parameter for governing LCF damage processes in Ni-SX superalloys.

4.4. The potential application of the multimodal 3D X-ray microscopy method

Fatigue damage research in Ni-SX superalloys has long been confined to conventional surface techniques, which simplify analysis due to the absence of 3D vision, thus increasing the uncertainty of established failure criteria [15, 16, 20, 60, 61]. Nevertheless, large-scale 3D measurements often encounter obstacles such as lengthy data acquisition times and the generation of excessively large datasets [62-64], especially considering the scarcity and periodic availability at synchrotron facilities. To overcome these limitations, this study adopted a combined approach: laboratory-based X-ray microtomography was first used for comprehensive microstructural imaging, followed by targeted low-dimensional characterization and preliminary analysis of damage micromechanisms. Synchrotron measurements were subsequently performed outside the crack-tip plasticity zone to evaluate local stress states in fatigued microstructures, further validating 2D-derived failure theories. This integrated methodology proves instrumental in identifying and analyzing the micromechanisms of deformation under load in cast materials with dendrite structures, such as aluminum cast alloys, certain austenitic cast steels, and copper cast alloys, while optimizing the utilization of synchrotron resources.

5. Conclusions

This study conducted LCF testing on the Ni-SX superalloy DD413 at 760 °C. Post-mortem and ~40%-fatigue-interrupted specimens were analyzed using a multimodal 3D X-ray microscopy approach integrating synchrotron 3D-μXRD, laboratory μ-CT, and complementary electron microscopy (EBSD, SEM-FIB, STEM). This methodology revealed submicron-resolution 3D distributions of dendritic microstructures, residual stress/strain fields, and solidification defects during both early fatigue damage and final failure. It also uncovered the mechanical heterogeneity inherent in the fatigue micromechanisms of the DD413 alloy. The study validates the synergistic use of 3D-μXRD and μ-CT and provides critical datasets and insights to advance multiphysics fatigue models and guide the design of novel fatigue-resistant single-crystal superalloys. The main conclusions are as follows:

1. Under intermediate-temperature LCF loading, the DCs and IDs of the DD413 superalloy exhibit heterogeneous microscale mechanical responses: the DCs accumulate local irreversible slip along specific slip systems to generate slip bands, while the IDs accommodate local microplasticity around intrinsic defects by activating multiple slip systems.
2. Local tensile stress near defects in the IDs is more than three times higher than in the slip bands of the DCs, driving the generation of local fatigue damage zones in the IDs. The chain-like distribution of defects promotes the interconnection of these local damage zones into continuous damage regions, resulting in an overall increase in tensile stress levels in the IDs.
3. GND density alone is insufficient to indicate LCF damage; both the internal stress state (tension or compression) and its magnitude must be considered.
4. Macroscale μ-CT effectively guides 3D-μXRD measurements by targeting critical structural features,

while high-resolution μ-CT aids in interpreting internal diffraction signals for correlative analysis. The combined use of multimodal μ-CT and 3D-μXRD enables accurate localization of internal damage zones within bulk fatigued Ni-SX superalloy and provides correlated 3D mapping of residual stress/strain fields, dendritic microstructures, and defects at the submicron scale across various regions.

References

1 T.M. Pollock, S. Tin, Nickel-based superalloys for advanced turbine engines: chemistry, microstructure and properties, ***J. Propul. Power*** 22 (2) (2006) 361-374.

2 T.M. Pollock, Alloy design for aircraft engines, ***Nat. Mater.*** 15 (8) (2016) 809-815.

3 R.C. Reed, T. Tao, N. Warnken, Alloys-by-design: application to nickel-based single crystal superalloys, ***Acta Mater.*** 57 (19) (2009) 5898-5913.

4 X. Wu, S.K. Makineni, C.H. Liebscher, G. Dehm, J. Rezaei Mianroodi, P. Shanthraj, B. Svendsen, D. Bürger, G. Eggeler, D. Raabe, B. Gault, Unveiling the Re effect in Ni-based single crystal superalloys, ***Nat. Commun.*** 11 (1) (2020) 389.

5 W. Xia, X. Zhao, L. Yue, Z. Zhang, A review of composition evolution in Ni-based single crystal superalloys, ***J. Mater. Sci. Technol.*** 44 (2020) 76-95.

6 C. Yang, Q. Xu, X. Su, B. Liu, Multiphase-field and experimental study of solidification behavior in a nickel-based single crystal superalloy, ***Acta Mater.*** 175 (2019) 286-296.

7 A. Heckl, R. Rettig, S. Cenanovic, M. Göken, R. Singer, Investigation of the final stages of solidification and eutectic phase formation in Re and Ru containing nickel-base superalloys, ***J. Cryst. Growth*** 312 (14) (2010) 2137-2144.

8 Z. Zhou, R. Li, Y. Wang, T. Li, S. Wang, S. Li, G. Xie, J. Zhang, Y.-D. Wang, Microscopic heterogeneity of low cyclic fatigue damage in Ni-based single crystal superalloy DD413, ***Mater. Charact.*** 207 (2024) 113551.

9 G. Liu, J.S. Cantó, S. Winwood, K. Rhodes, S. Birosca, The effects of microstructure and microtexture generated during solidification on deformation micromechanism in IN713C nickel-based superalloy, ***Acta Mater.*** 148 (2018) 391-406.

10 G. Liu, S. Winwood, K. Rhodes, S. Birosca, The effects of grain size, dendritic structure and crystallographic orientation on fatigue crack propagation in IN713C nickel-based superalloy,

Int. J. Plast. 125 (2020) 150-168.

11 A. Pineau, D.L. McDowell, E.P. Busso, S.D. Antolovich, Failure of metals II: Fatigue, ***Acta Mater.*** 107 (2016) 484-507.

12 J.J. Kruzic, Predicting Fatigue Failures, ***Science*** 325 (5937) (2009) 156-158.

13 S. Lavenstein, Y. Gu, D. Madisetti, J.A. El-Awady, The heterogeneity of persistent slip band nucleation and evolution in metals at the micrometer scale, ***Science*** 370 (6513) (2020) eabb2690.

14 S. Steuer, P. Villechaise, T.M. Pollock, J. Cormier, Benefits of high gradient solidification for creep and low cycle fatigue of AM1 single crystal superalloy, ***Mater. Sci. Eng., A*** 645 (2015) 109-115.

15 B. Ruttert, C. Meid, L.M. Roncery, I. Lopez-Galilea, M. Bartsch, W. Theisen, Effect of porosity and eutectics on the high-temperature low-cycle fatigue performance of a nickel-base single-crystal superalloy, ***Scr. Mater.*** 155 (2018) 139-143.

16 X. Ma, H.-J. Shi, In situ SEM studies of the low cycle fatigue behavior of DZ4 superalloy at elevated temperature: Effect of partial recrystallization, ***Int. J. Fatigue*** 61 (2014) 255-263.

17 D. Texier, J.-C. Stinville, M.-A. Charpagne, Z. Chen, V. Valle, P. Villechaise, T.M. Pollock, J. Cormier, Role of non-metallic inclusions and twins on the variability in fatigue life in alloy 718 nickel base superalloy, ***Superalloys*** 2020: Proceedings of the 14th International Symposium on Superalloys, Springer, 2020, pp. 629-639.

18 J. Jiang, J. Yang, T. Zhang, F.P.E. Dunne, T.B. Britton, On the mechanistic basis of fatigue crack nucleation in Ni superalloy containing inclusions using high resolution electron backscatter diffraction, ***Acta Mater.*** 97 (2015) 367-379.

19 R. Jiang, D.J. Bull, A. Evangelou, A. Harte, F. Pierron, I. Sinclair, M. Preuss, X.T. Hu, P.A.S. Reed, Strain accumulation and fatigue crack initiation at pores and carbides in a SX superalloy at room temperature, ***Int. J. Fatigue*** 114 (2018) 22-33.

20 X. Ren, J. Lu, J. Zhou, X. Liu, W. Jiang, J. Wang, Y. Zhang, Z. Zhang, In-situ fatigue behavior study of a nickel-based single-crystal superalloy with different orientations, ***Mater. Sci. Eng., A*** 855 (2022) 143913.

21 J.C. Stinville, P.G. Callahan, M.A. Charpagne, M.P. Echlin, V. Valle, T.M. Pollock, Direct measurements of slip irreversibility in a nickel-based superalloy using high resolution digital

image correlation, ***Acta Mater.*** 186 (2020) 172-189.

22 G. Liu, L. Kong, S. Ruan, S. Birosca, Microstructure and phases structure in nickel-based superalloy IN713C after solidifications, ***Mater. Charact***. 182 (2021) 111566.

23 R. Li, Q. Xie, Y.-D. Wang, W. Liu, M. Wang, G. Wu, X. Li, M. Zhang, Z. Lu, C. Geng, T. Zhu, Unraveling submicron-scale mechanical heterogeneity by three-dimensional X-ray microdiffraction, ***PNAS*** 115 (3) (2018) 483-488.

24 Z. Guo, X. Lu, C. Paramatmuni, H. Gao, F.P.E. Dunne, W. Yan, Y.-W. Zhang, Y. Xu, Slip system-resolved GNDs and SEDs: A multi-scale framework for predicting crack nucleation in single-crystal metals, ***Acta Mater.*** 288 (2025) 120853.

25 Z. Liu, Z. Zhao, T. Zheng, J. Mu, G. Xie, J. Zhang, L. He, Y. Wang, A mechanism on multiscale heterogenous deformation of nickel-based single crystal superalloys unraveled by time-of-flight neutron diffraction technology, ***Acta Mater.*** 281 (2024) 120430.

26 T. Swift, Damage tolerance capability, ***Int. J. Fatigue*** 16 (1) (1994) 75-94.

27 M.M. Omar, J.A. El-Awady, Foreseeing metal failure from its inception, ***Science*** 377 (6610) (2022) 1047-1048.

28 R. Li, Y.-D. Wang, W. Liu, C. Geng, Q. Xie, D.E. Brown, K. An, Multiscale mechanical fatigue damage of stainless steel investigated by neutron diffraction and X-ray microdiffraction, ***Acta Mater.*** 165 (2019) 336-345.

29 Z. Yan, K. Srikakulapu, Y. Gao, H. Qin, Y. Rong, Z. Bi, Q. Xie, K. An, Y.-d. Wang, Q. Tan, γ′-size effect on the deformation microstructure and texture in a Ni-based superalloy using in-situ neutron diffraction, ***Scr. Mater.*** 236 (2023) 115665.

30 Z. Zhang, Y. Feng, Q. Tan, J. Zou, J. Li, X. Zhou, G. Sun, Y. Wang, Residual stress distribution in Ni-based superalloy turbine discs during fabrication evaluated by neutron/X-ray diffraction measurement and thermomechanical simulation, ***Mater. Des.*** 166 (2019) 107603.

31 Z. Zhu, C. Xiong, J. Wang, R. Li, Y. Ren, Y. Wang, Y. Li, In situ synchrotron X-ray diffraction investigations of the physical mechanism of ultra-low strain hardening in Ti-30Zr-10Nb alloy, ***Acta Mater.*** 154 (2018) 45-55.

32 T. Britton, J. Hickey, Understanding deformation with high angular resolution electron backscatter diffraction (HR-EBSD), IOP Conference Series: Materials Science and Engineering,

IOP Publishing, 2018, p. 012003.

33 S. Kalácska, J. Ast, P.D. Ispánovity, J. Michler, X. Maeder, 3D HR-EBSD Characterization of the plastic zone around crack tips in tungsten single crystals at the micron scale, ***Acta Mater.*** 200 (2020) 211-222.

34 P.J. Withers, C. Bouman, S. Carmignato, V. Cnudde, D. Grimaldi, C.K. Hagen, E. Maire, M. Manley, A. Du Plessis, S.R. Stock, X-ray computed tomography, ***Nat. Rev. Methods Primers*** 1 (1) (2021) 18.

35 B.C. Larson, W. Yang, G.E. Ice, J.D. Budai, J.Z. Tischler, Three-dimensional X-ray structural microscopy with submicrometre resolution, ***Nature*** 415 (6874) (2002) 887-890.

36 M. Herbig, A. King, P. Reischig, H. Proudhon, E.M. Lauridsen, J. Marrow, J.-Y. Buffière, W. Ludwig, 3-D growth of a short fatigue crack within a polycrystalline microstructure studied using combined diffraction and phase-contrast X-ray tomography, ***Acta Mater.*** 59(2) (2011) 590-601.

37 H. Simons, A. King, W. Ludwig, C. Detlefs, W. Pantleon, S. Schmidt, F. Stöhr, I. Snigireva, A. Snigirev, H.F. Poulsen, Dark-field X-ray microscopy for multiscale structural characterization, ***Nat. Commun.*** 6 (1) (2015) 6098.

38 Y. Hu, S. Wu, Y. Guo, Z. Shen, A.M. Korsunsky, Y. Yu, X. Zhang, Y. Fu, Z. Che, T. Xiao, S. Lozano-Perez, Q. Yuan, X. Zhong, X. Zeng, G. Kang, P.J. Withers, Inhibiting weld cracking in high-strength aluminium alloys, ***Nat. Commun.*** 13 (1) (2022) 5816.

39 P.M. Sarosi, J. Furmanski, W.C. Reese, D.L. Carpenter, M.A. Nittoli, M.G. Myers, N.M. Callen, T. Neeraj, Damage evolution during fracture by correlative microscopy with hyperspectral electron microscopy and laboratory-based microtomography, ***Sci. Adv.*** 8 (14) (2022) eabj6738.

40 E.F.F. Knipschildt, X. Lei, Y.B. Zhang, T. Yu, S. Fæster, W. Liu, R.E. Sanders, D. Juul Jensen, Registration of data from a multimodal investigation of particle stimulated nucleation in aluminum, IOP Conference Series: Materials Science and Engineering 1249 (1) (2022) 012049.

41 F. Bachmann, R. Hielscher, H. Schaeben, Grain detection from 2d and 3d EBSD data—Specification of the MTEX algorithm, ***Ultramicroscopy*** 111 (12) (2011) 1720-1733.

42 A. Poshadel, P. Dawson, G. Johnson, Assessment of deviatoric lattice strain uncertainty for polychromatic X-ray microdiffraction experiments, ***J. Synchrotron Radiat.*** 19 (2) (2012) 237-

244.

43 W. Pantleon, Resolving the geometrically necessary dislocation content by conventional electron backscattering diffraction, ***Scr. Mater.*** 58 (11) (2008) 994-997.

44 O. Muransky, L. Balogh, M. Tran, C. Hamelin, J.-S. Park, M.R. Daymond, On the measurement of dislocations and dislocation substructures using EBSD and HRSD techniques, ***Acta Mater.*** 175 (2019) 297-313.

45 J.F. Nye, Some geometrical relations in dislocated crystals, ***Acta Metall.*** 1 (2) (1953) 153-162.

46 P.S. Karamched, A.J. Wilkinson, High resolution electron backscatter diffraction analysis of thermally and mechanically induced strains near carbide inclusions in a superalloy, ***Acta Mater.*** 59 (1) (2011) 263-272.

47 R. Hielscher, C.B. Silbermann, E. Schmidl, J. Ihlemann, Denoising of crystal orientation maps, ***J. Appl. Crystallogr.*** 52 (5) (2019) 984-996.

48 A. Piglione, T. Bellamy, J. Yu, J. Zhao, C. Xiao, F.P. Dunne, M.-S. Pham, Dislocation arrangements and cyclic microplasticity surrounding stress concentration in a Ni-based single-crystal superalloy, ***Adv. Eng. Mater.*** 26 (1) (2024) 2300602.

49 T. Yu, Y. Du, G. Fan, R. Xu, R. Barabash, N. Hansen, X. Huang, Y. Zhang, In-situ synchrotron X-ray micro-diffraction investigation of ultra-low-strain deformation microstructure in laminated Ti-Al composites, ***Acta Mater.*** 202 (2021) 149-158.

50 L. Zhang, L. Zhao, A. Roy, V. Silberschmidt, G. Mccolvin, Low-cycle fatigue of single crystal nickel-based superalloy–mechanical testing and TEM characterisation, ***Mater. Sci. Eng., A*** 744 (2019) 538-547.

51 X. Chen, Q. Wang, Z. Cheng, M. Zhu, H. Zhou, P. Jiang, L. Zhou, Q. Xue, F. Yuan, J. Zhu, X. Wu, E. Ma, Direct observation of chemical short-range order in a medium-entropy alloy, ***Nature*** 592 (7856) (2021) 712-716.

52 J.S. Cantó, S. Winwood, K. Rhodes, S. Birosca, A study of low cycle fatigue life and its correlation with microstructural parameters in IN713C nickel based superalloy, ***Mater. Sci. Eng., A*** 718 (2018) 19-32.

53 K. Pang, H. Yuan, Fatigue life assessment of a porous casting nickel-based superalloy based on fracture mechanics methodology, ***Int. J. Fatigue*** 136 (2020) 105575.

54 A.J. Allen, H.M. T., W.C. G., C. and Andreani, Neutron diffraction methods for the study of residual stress fields, ***Adv. Phys***. 34(4) (1985) 445-473.

55 P.E. Aba-Perea, T. Pirling, P.J. Withers, J. Kelleher, S. Kabra, M. Preuss, Determination of the high temperature elastic properties and diffraction elastic constants of Ni-base superalloys, ***Mater. Des***. 89 (2016) 856-863.

56 J. Jiang, J. Yang, T. Zhang, J. Zou, Y. Wang, F. Dunne, T. Britton, Microstructurally sensitive crack nucleation around inclusions in powder metallurgy nickel-based superalloys, ***Acta Mater.*** 117 (2016) 333-344.

57 V. Wan, J. Jiang, D. MacLachlan, F. Dunne, Microstructure-sensitive fatigue crack nucleation in a polycrystalline Ni superalloy, ***Int. J. Fatigue*** 90 (2016) 181-190.

58 A.N. Stroh, A theory of the fracture of metals, ***Adv. Phys.*** 6 (24) (1957) 418-465.

59 J.C. Stinville, N. Vanderesse, F. Bridier, P. Bocher, T.M. Pollock, High resolution mapping of strain localization near twin boundaries in a nickel-based superalloy, ***Acta Mater.*** 98 (2015) 29-42.

60 A. Cervellon, S. Hémery, P. Kürnsteiner, B. Gault, P. Kontis, J. Cormier, Crack initiation mechanisms during very high cycle fatigue of Ni-based single crystal superalloys at high temperature, ***Acta Mater.*** 188 (2020) 131-144.

61 A. Cervellon, C.J. Torbet, T.M. Pollock, Crack initiation anisotropy of Ni-based SX superalloys in the very high cycle fatigue regime, ***Mater. Sci. Eng., A*** 825 (2021) 141920.

62 S. Gustafson, W. Ludwig, P. Shade, D. Naragani, D. Pagan, P. Cook, C. Yildirim, C. Detlefs, M.D. Sangid, Quantifying microscale drivers for fatigue failure via coupled synchrotron X-ray characterization and simulations, ***Nat. Commun.*** 11 (1) (2020) 3189.

63 M. Arul Kumar, B. Clausen, L. Capolungo, R.J. McCabe, W. Liu, J.Z. Tischler, C.N. Tomé, Deformation twinning and grain partitioning in a hexagonal close-packed magnesium alloy, ***Nat. Commun.*** 9 (1) (2018) 4761.

64 T.L. Burnett, P.J. Withers, Completing the picture through correlative characterization, ***Nat. Mater.*** 18 (10) (2019) 1041-1049.

Acknowledgments

We thank Z.R. Yan, R. Liu, and X.Y. Jin for their assistance in the experiment. This work was supported by the National Key Research and Development Program of China (Grant No. 2021YFA1600600), the National Natural Science Foundation of China (NSFC) (No.s U2141206, 51921001), the Fundamental Research Funds for the Central Universities (Grant No. FRF-BD-20-02B), the fundamental research fund at the State Key Laboratory for Advanced Metals and Materials (2021Z-05, 2022Z-02), and the Guangdong-Hong Kong-Macao Joint Laboratory for Neutron Scattering Science and Technology. The use of the Advanced Photon Source was supported by the US Department of Energy, Office of Science, Office of Basic Energy Sciences, under Contract No. DE-AC02-06CH11357.

Author contributions

Y-.W., W.L., J.C. and Q.F. designed the research and advised on manuscript preparation. Z.Z., W.L. and G. C. conducted mechanical, TEM and μ-CT experiments with assistance from C.S., J.Z. and S.L. Z.Z., Y.W., R.L. and Y-.W. analyzed the data and wrote the original draught with input from all co-authors. R. L., S. L., and W.L. conducted synchrotron-based experiments. All co-authors discussed the results and performed activities in writing, reviewing and editing the manuscript. Y-.W. supervised the project.

Competing interests

The authors declare no competing interests.

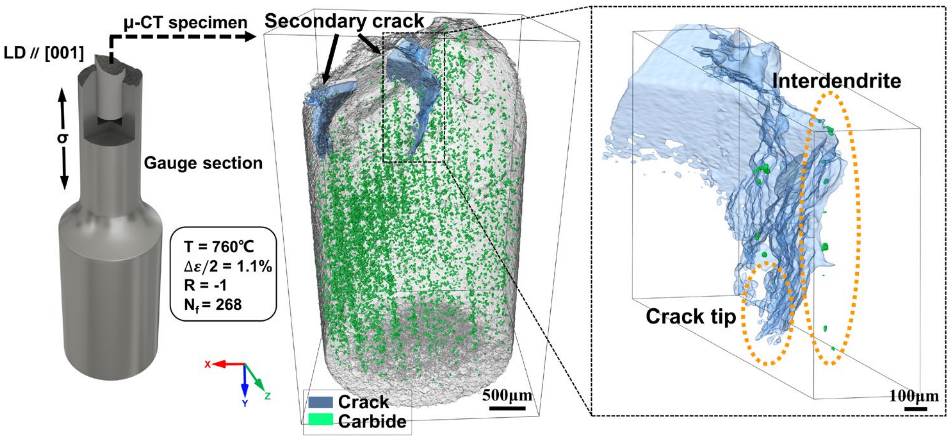

Fig. 1. Post-mortem micro-computed tomography (μ-CT) captured the distribution of secondary cracks and carbides within the miniature sample. The crack path is displayed on the right from a 3D perspective.

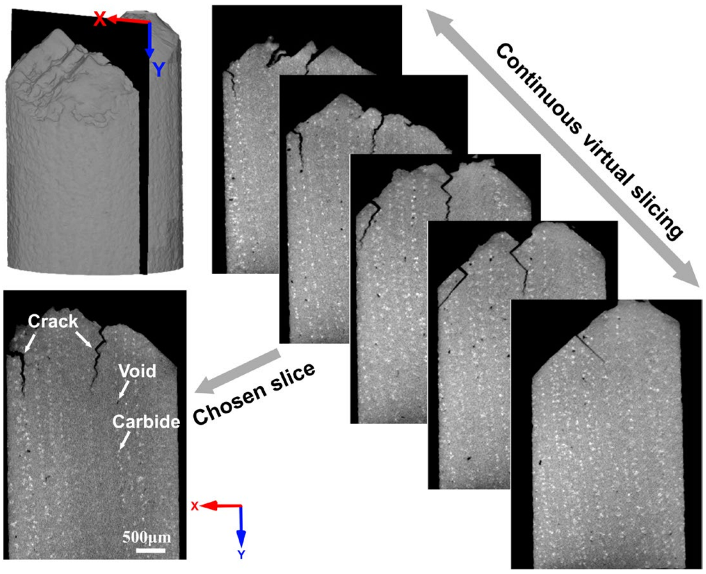

Fig. 2. μ-CT slices parallel to the X-Y plane reveal a microcrack path aligned with chain-like intrinsic defects. The carbides and voids appear in a representative slice as white and black spots.

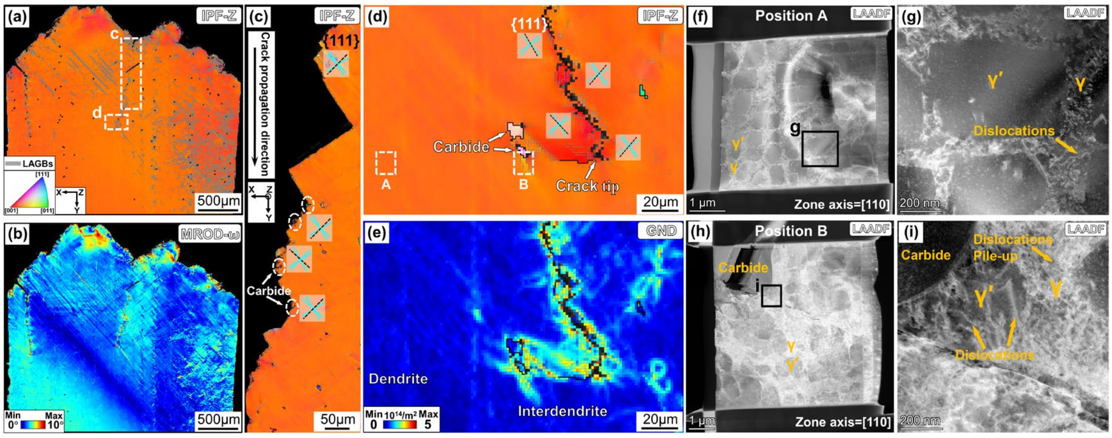

Fig. 3. EBSD analysis of the selected slice. (a) IPF-Z map superimposed with LAGBs. (b) MROD-ω map of **a**. (c) A magnified view in **a** illustrates the short crack growth influenced by carbides, overlayed with {111} traces. (d) A magnified view of the crack tip region in **a** with arrows indicating the carbides to which the crack tip turned. (e) GND density map of **d**. LAADF STEM imaging discerns dislocation configurations in region A (f, g) and region B (h, i) (as indicated by white dashed rectangles in **d**).

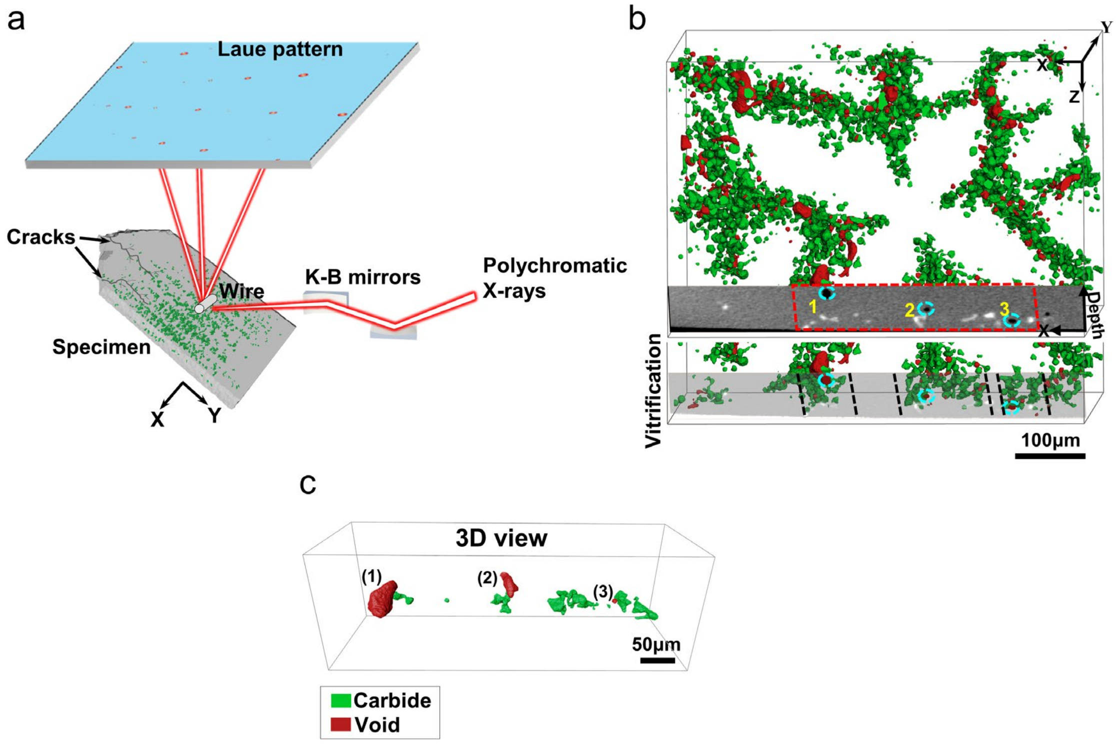

Fig. 4. Spatially correlating 3D-μXRD and μ-CT to analyze crystallographic orientation and elastic strain fields. (a) Schematic of 3D-μXRD setup. (b) The coverage of the 3D-μXRD scan inside the specimen (depicted by the red dashed rectangle) includes three voids (outlined by blue dashed line) for registering the μ-CT slice, with the lower semitransparent cross-section highlighting dendrites (DCs) and interdendrites (IDs) subdivided by black dashed lines. (c) 3D morphology of intrinsic defects on the 3D-μXRD cross-section.

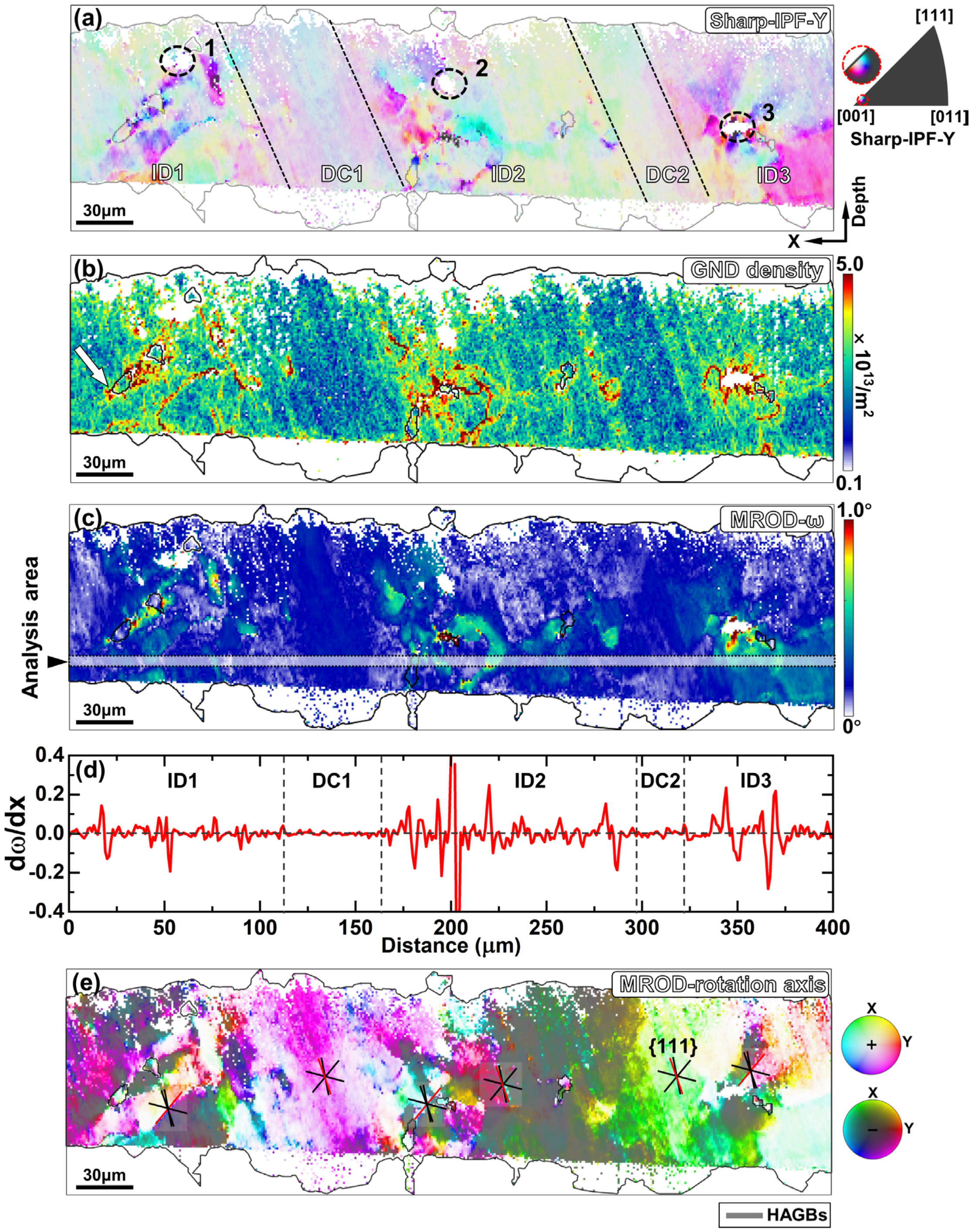

Fig. 5. 3D-μXRD crystallographic orientation fields. (a) IPF-Y within a ~1° range (Sharp-IPF-Y) coloring map containing three registered voids, superimposed with HAGBs, DCs (DC1, DC2) and IDs (ID1, ID2, ID3) are subdivided by black dashed lines. (b) GND density map. (c) MROD-ω map. (d) Derivative of MROD-ω along the X-direction in a bright white dashed rectangle (indicated by the black arrow in **c**). (e) MROD-ω axes map superimposed with {111} slip traces. X, Y, Z, and depth denote the transverse, loading, normal, and 45° incidence directions concerning the sample surface in the specimen frame.

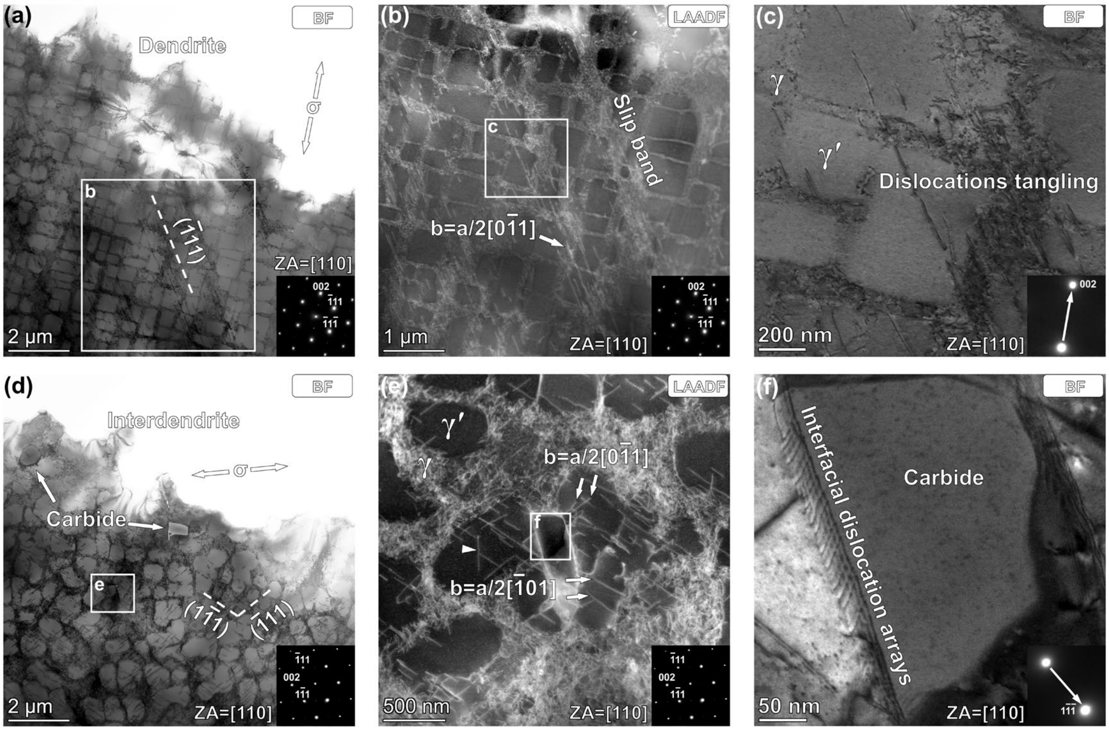

Fig. 6. Dislocation configurations near the 3D-μXRD cross-section. (a) BF STEM imaging in the DC. (b) LAADF STEM imaging of a magnified view in **a**. (c) BF STEM imaging of a magnified view in **b**. (d) BF STEM imaging in ID. (e) LAADF STEM imaging of a magnified view in **d**. (f) BF STEM imaging of a magnified view in **e**. Zone axis: [110] for **a**-**f**. g vector: [002] for **c** and $[1\bar{1}\bar{1}]$ for **f**.

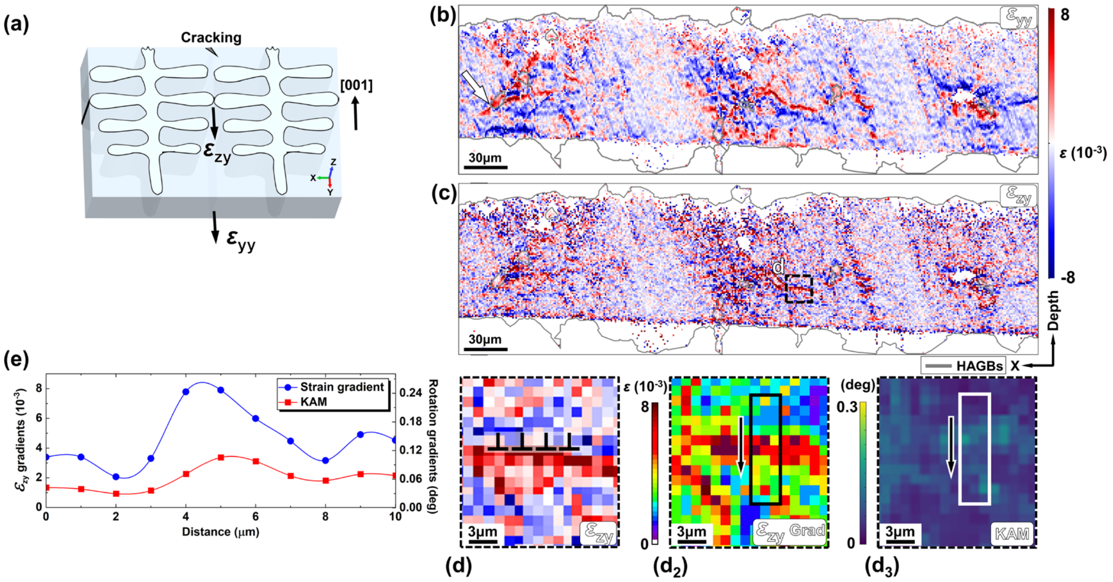

Fig. 7. 3D-μXRD elastic strain fields. (a) Schematic of elastic strain components in the sample frame. (b) Normal elastic strain component ε_{yy} map. (c) Shear elastic strain component ε_{zy} map. (d) The magnified view in **c** is superimposed with the dislocation pile-up configuration corresponding to the tensile and compressive stress zones. (d_2) Shear elastic strain gradient (ε_{zy} Grad) map of **d**. (d_3) KAM map of **d**. (e) Variations in ε_{zy} Grad and KAM across the elastic strain transition zone (indicated by black and white rectangles in **d₂** and **d₃**), with arrows indicating increasing distance.

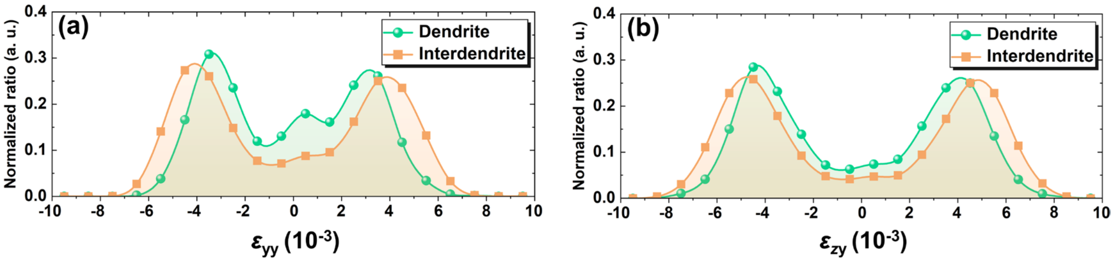

Fig. 8. (a) Distribution of ε_{yy} in DCs and IDs. (b) Distribution of ε_{zy} in DCs and IDs.

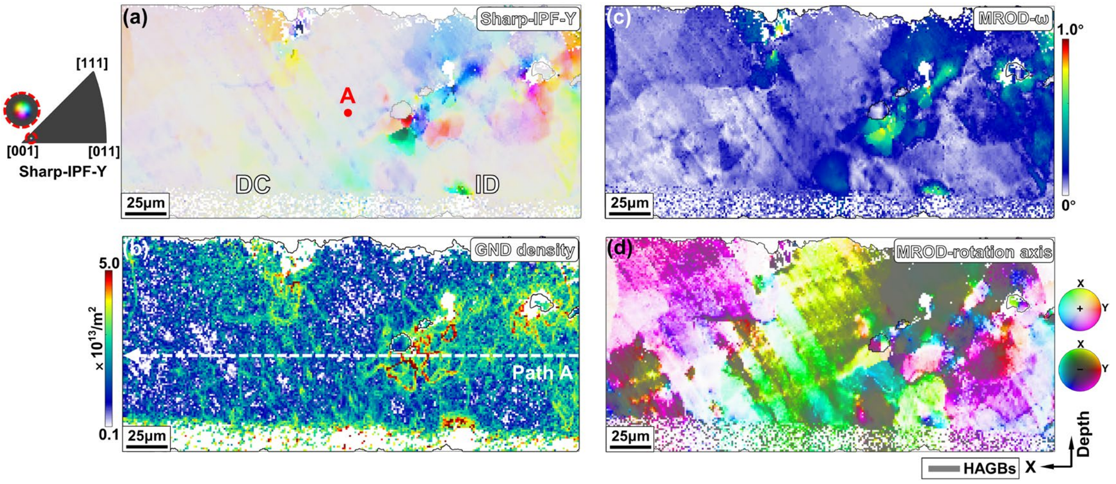

Fig. 9. 3D-μXRD crystallographic orientation fields for samples interrupted at ~40% of LCF life. (a) Sharp-IPF-Y coloring map, superimposed with HAGBs. DC and ID are subdivided by a black dashed line. (b) GND density map. (c) MROD-ω map. (d) MROD-ω axes map. X, Y, Z, and depth denote the transverse, loading, normal, and 45° incidence directions concerning the sample surface in the specimen frame.

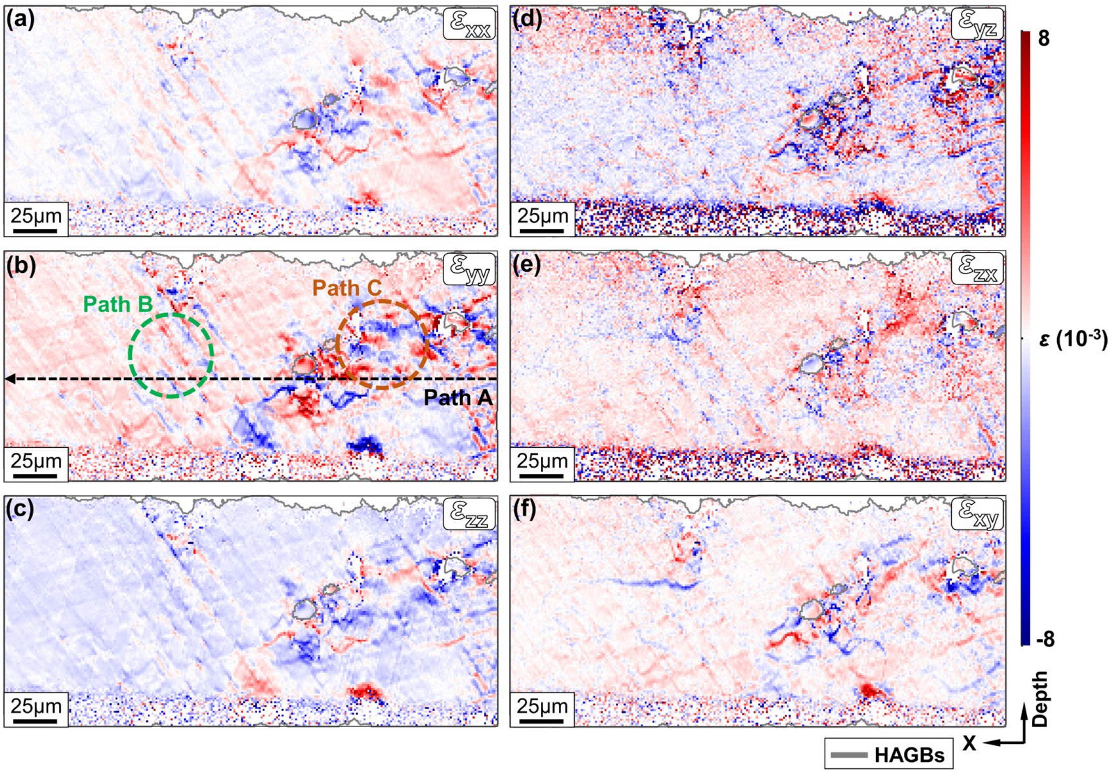

Fig. 10. 3D-μXRD elastic strain component maps for samples interrupted at ~40% of LCF life. (a) ε_{xx}. (b) ε_{yy}. (c) ε_{zz}. (d) ε_{yz}. (e) ε_{zx}. (f) ε_{xy}.

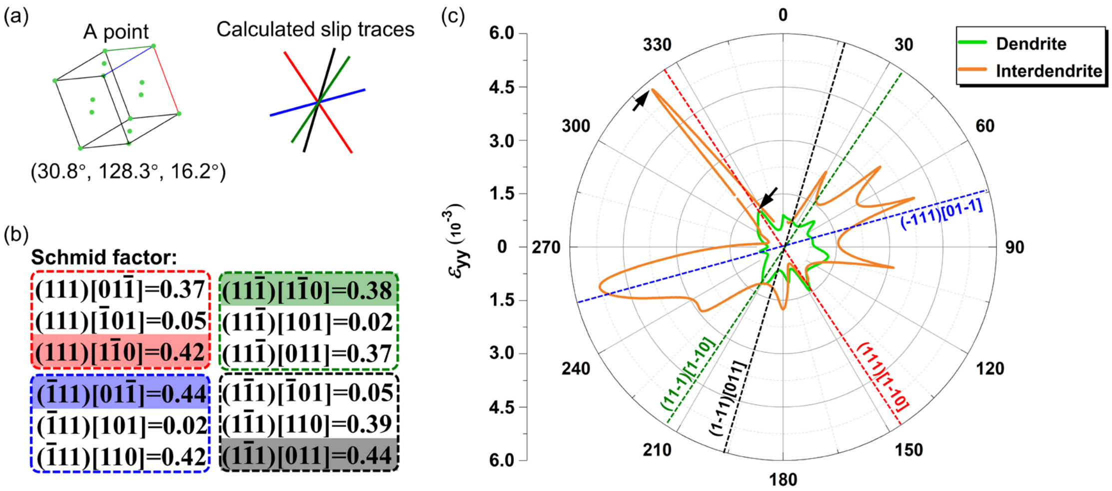

Schmid factor:

$(111)[01\bar{1}]=0.37$
$(111)[\bar{1}01]=0.05$
$(111)[1\bar{1}0]=0.42$

$(11\bar{1})[1\bar{1}0]=0.38$
$(11\bar{1})[101]=0.02$
$(11\bar{1})[011]=0.37$

$(\bar{1}11)[01\bar{1}]=0.44$
$(\bar{1}11)[101]=0.02$
$(\bar{1}11)[110]=0.42$

$(1\bar{1}1)[\bar{1}01]=0.05$
$(1\bar{1}1)[110]=0.39$
$(1\bar{1}1)[011]=0.44$

Fig. 11. Quantitative comparison of fatigue damage modes between DCs and IDs. (a) Slip traces calculated from the crystallographic orientation (Euler angles) at Point A in Fig. 9a. (b) Comparison of the Schmid factors for different slip systems at Point A. (c) Comparison of the distributions of ε_{yy} (considering only tensile components) along Paths B and C in Fig. 10b, overlaid with slip traces.

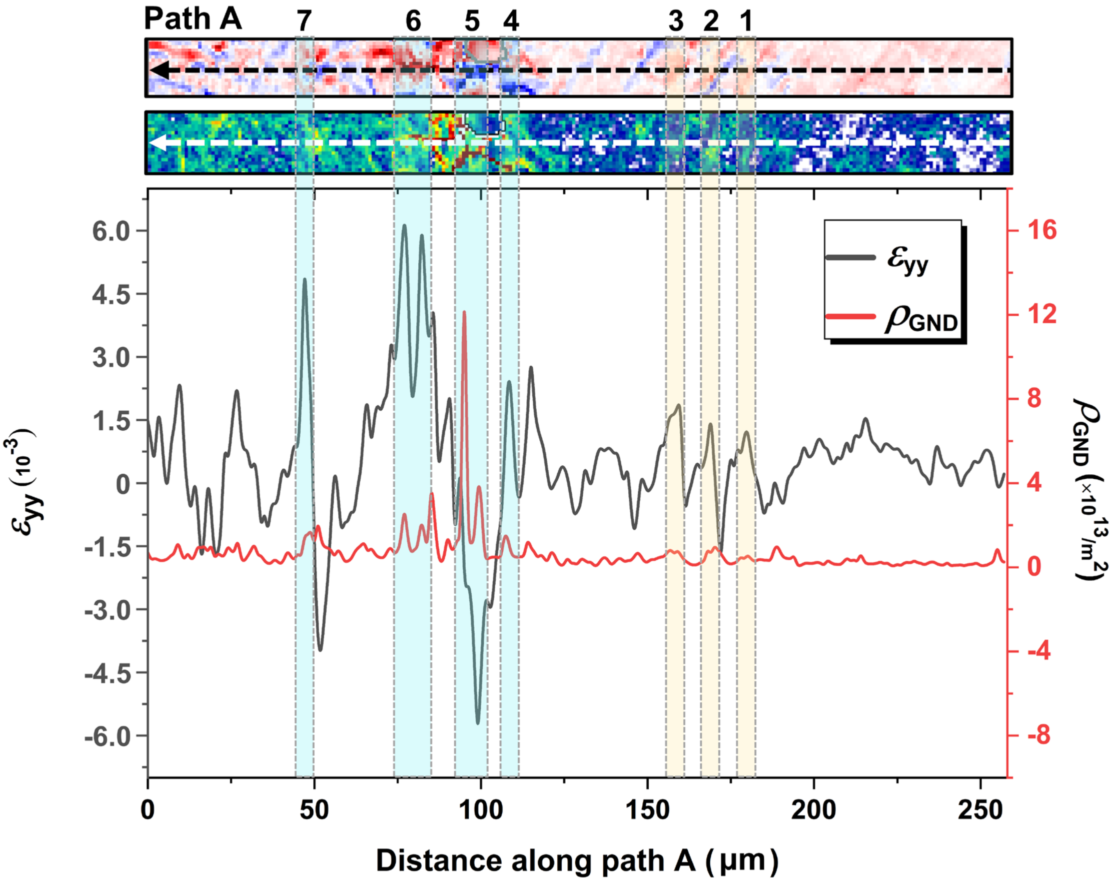

Fig. 12. Quantitative comparison of ε_{yy} and GND density along Path A in Figs. 9b and 10b.

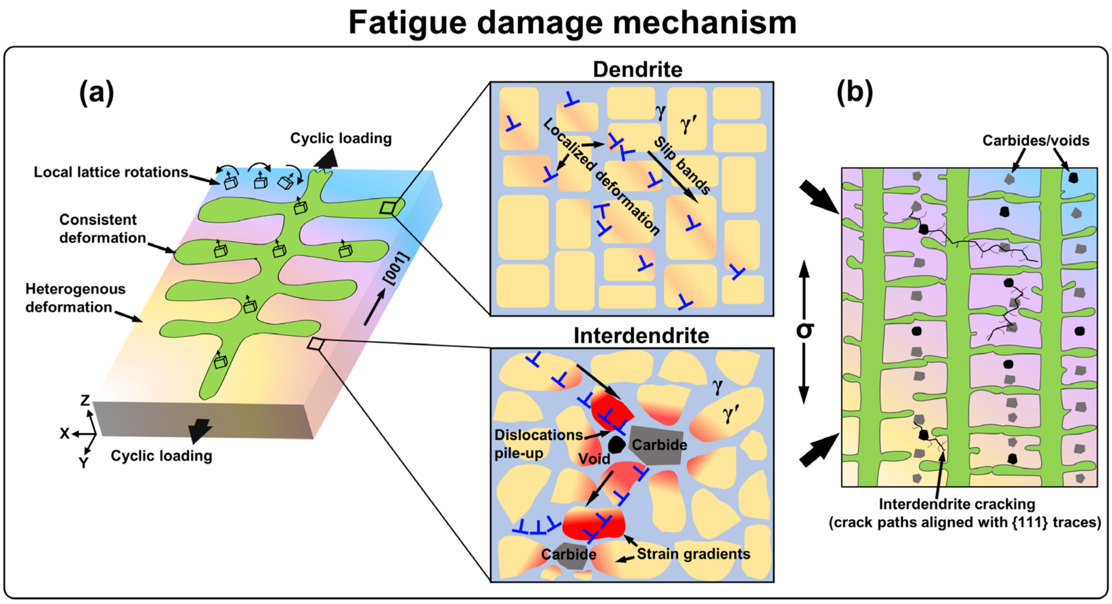

Fig. 13. Schematic of the heterogeneous fatigue damage mechanism. (a) DCs represented by a homogeneous color indicating consistent orientation showcase a unidirectionally aligned dislocation configuration with a relatively mild banded elastic strain field. IDs characterized by varied colors suggesting fluctuating orientation reveal dislocation pile-ups from various slip systems and sharp elastic strain gradients around intrinsic defects. (b) Chain-like intrinsic defects within IDs can result in extensive fatigue cracking aligned with {111} slip traces.

Table 1. Chemical compositions of the Ni-SX superalloy DD413 (wt.%).

C	Cr	Co	W	Mo	Al	Ti	Ta	Ni
0.05~0.1	11.5~12.5	8.5~9.5	3.5~4.5	1.5~2.5	3.0~4.0	3.5~4.5	4.5~5.5	Bal.

Table 2. Crystallographic parameters of the matrix and carbides.

Phase	Space group	lattice parameter/nm
MC carbide	Fm-3m	0.4340
γ	Fm-3m	0.3664
γ'	Pm-3m	0.3580

Table 3. Detailed explanations of the main abbreviations in the text.

Acronyms	Interpretations
DC	Dendrite core region
ID	Interdendritic region
MROD-ω	Grain reference orientation deviation angle
GND	Geometrically necessary dislocation
KAM	Kernel average misorientation